

Morphology of Fe/MgO(001) ultrathin films

Rüdiger Reitinger,^{a)} Bogdan Sepiol, and Gero Vogl
Faculty of Physics, University of Vienna, Strudlhofgasse 4, 1090 Vienna, Austria

Bastian Pfau
²*Faculty of Physics, University of Vienna, Strudlhofgasse 4, 1090 Vienna, Austria*
and
BESSY GmbH, Albert-Einstein-Straße 15, 12489 Berlin, Germany

Lorenz-Mathias Stadler
⁴*Faculty of Physics, University of Vienna, Strudlhofgasse 4 1090 Vienna, Austria*
and
HASYLAB at DESY, Notkestraße 85, 22607 Hamburg, Germany

Svetoslav Stankov and Federico Zontone
European Synchrotron Radiation Facility, BP 220, 38043 Grenoble Cedex, France

Nika Spiridis
Institute of Catalysis and Surface Chemistry, PAN, ul. Niezapominajek 8, 30-239 Cracow, Poland

Józef Korecki
Institute of Catalysis and Surface Chemistry, PAN, ul. Niezapominajek 8, 30-239 Cracow, Poland
and *Department of Solid State Physics, Faculty of Physics and Applied Computer Science, AGH, University of Science and Technology, al. Mickiewicza 30, 30-059 Cracow, Poland*

(Received 30 May 2007; accepted 10 June 2007; published online 13 August 2007)

The structural and magnetic properties of iron clusters resulting from the evaporation of five monolayers of iron on a polished MgO(001) substrate are examined by grazing-incidence small-angle x-ray scattering, and conversion electron Mössbauer spectroscopy. Volmer-Weber-growth is observed for room-temperature deposition, giving rise to spherical, superparamagnetic islands. Subsequent annealing causes coarsening and the particles become hemispherical. In the early stages of annealing cluster diffusion takes place, whereas later, Ostwald ripening is the dominant coarsening mechanism. The diffusion coefficient is independent from the crystallographic directions in the MgO(001) surface as it is proven by the isotropic island distribution and shape. The superparamagnetic state of the particles is conserved during the whole annealing process. For ultrathin iron layers we show that, in contrast to bulk iron, the Curie temperature lies well below room temperature. © 2007 American Institute of Physics. [DOI: 10.1063/1.2760844]

I. INTRODUCTION

Iron on MgO(001) is both of fundamental and technical interest for various reasons. For instance, thin layers and multilayers of iron have extraordinary and potentially useful magnetic properties related to their structures.¹ According to theoretical predictions, MgO is supposed to be an ideal substrate for model thin iron films, since the magnetic moment of an iron monolayer (ML) on MgO(001) has been calculated to be $3.07 \mu_B$ at 0 K.² This value nearly reproduces the theoretical enhancement of the magnetic moment for a free-standing iron monolayer² ($3.1 \mu_B$), being much higher than that of bulk iron³ ($2.2 \mu_B$). On the other hand, the anticipated enhanced magnetic moment has not been confirmed experimentally. In fact, ultrathin iron films on MgO were found to be ferromagnetic, with a magnetic moment practically identical to that of bulk iron.⁴ A quite promising technical application is the fabrication of submicron iron particles⁵ and iron wires^{6,7} on MgO, as MgO is supposed to be an ideal substrate for iron due to the lattice mismatch of

only^{8,9} 3.5%–4%. However, most likely because of the difference in surface energies [Fe (Ref. 10): 2900 nJ/mm^2 , MgO (Ref. 9): 1200 nJ/mm^2], thin iron layers do not wet the MgO surface.⁹ Iron has been found to act as an appropriate seed layer for subsequent epitaxial deposition of other layers as well as multilayers.^{1,11,12}

Molecular beam epitaxy (MBE) of metals on oxide surfaces often leads to the Volmer-Weber growth mode: The initially deposited material exists in the form of distinct islands on the substrate. These coarsen and agglomerate as more material is deposited.¹ The growth of metal clusters is strongly influenced by surface diffusion, which allows for transport of material during the growth process.^{13,14} Above a critical temperature, the so-called Schwoebel barrier¹⁵ is overcome. This means that atoms can diffuse not only upward but also downward at step edges.^{13,16} Hence, Fe/MgO forms an ideal Schwoebel system.¹⁴ Deposition of 20 Å of iron at room temperature leads to the formation of round-shaped islands⁸ with a diameter of 50 Å typically. However, if the deposition temperature is raised to about 110 °C, square-shaped islands with a characteristic diagonal of approximately 100 Å develop. After deposition at tempera-

^{a)}Electronic mail: ruediger.reitinger@univie.ac.at

tures around 210 °C, annealing of the sample broadens the islands' height distribution and the size of the terraces on top of the islands.⁸ It has to be emphasized that in our survey the iron was deposited at room temperature and annealed subsequently.

As MgO is an insulator, it is only possible to use scanning tunneling microscopy (STM) as long as a continuous iron film exists on the sample surface. Therefore, separated islands cannot be observed using this method.⁸ Alternatively, atomic force microscopy (AFM),^{17,18} grazing-incidence small-angle x-ray scattering (GISAXS),^{19–21} and conversion electron Mössbauer spectroscopy (CEMS)²² can be used, since these methods work without any obligatory conducting surface. So far, AFM investigations for film thicknesses down to 1 nm are reported,¹⁸ albeit differences in sample preparation have to be taken into account, as these play a crucial role for the resulting structures.^{18,23,24} Furthermore, there is an essential difference between cleaved and polished MgO(001) surfaces. Due to polishing, impurities are introduced, which are most likely acting as nucleation centers for the iron.^{24,25} It has to be emphasized that for the survey presented here a polished substrate was used. This fact explains some differences between the results of this paper and former findings.²⁶ The aim of the present work is to reveal island growth processes during annealing as well as the magnetic properties of the clusters grown on polished MgO(001) substrates.

II. EXPERIMENTAL PROCEDURES

All experiments were performed in ultrahigh-vacuum (UHV) conditions. Polished MgO(001) substrates were mounted on a resistively heated molybdenum holder. After insertion into the UHV system the substrates were annealed for several hours at 800 K. Iron was deposited on the substrates kept at room temperature, either from a resistively heated Be crucible or from an electron bombardment source. The deposition rate was 1.5 Å/min. For the CEMS experiments ⁵⁷Fe was used. All investigated samples had a standard thickness of 5 ML (≈ 7 Å), as controlled with a quartz crystal oscillator. The growth process was monitored by low-energy electron diffraction (LEED). LEED images displaying broad spots indicated an imperfect film structure, pointing toward island or small grain morphology. Nevertheless, epitaxial relations between the deposit and the substrates could be unambiguously established as the following: The [110] direction of the Fe(001) layer is parallel to the [100] direction of the MgO(001) substrate. The evolution of the morphology and the chemical and structural state of the iron atoms due to annealing were characterized by GISAXS and CEMS. GISAXS data were collected at room temperature on the as-prepared sample and after annealing steps at temperatures between 100 °C and 550 °C for 30 min, each. Further measurements were performed after heat treatment at 550 °C for 30, 90, and 210 min, changing the azimuthal angle ψ of the sample between 0° and 45° with respect to the incidence beam. During the data acquisition and the annealing procedure the specimen temperature was controlled by a thermocouple mounted on the sample holder. All data were

simulated and fitted by the software ISGISAXS,²⁷ which is based on the distorted wave Born approximation.^{28–34} As interference function the one-dimensional paracrystal interference function was chosen.²⁷

CEMS spectra were recorded at room temperature and at 80 K from as-prepared and annealed samples. A different set of samples, although prepared in the same way, was used for the GISAXS studies performed at the high-brilliance undulator beamline ID10A at the European Synchrotron Radiation Facility (ESRF) in Grenoble, France. We used an x-ray energy of 8 keV ($\lambda = 1.55$ Å). A circular pinhole with a diameter of $d = 12$ μm was placed 25 cm upstream the specimen. Parasitic scattering produced by the pinhole was shielded by guard slits.³⁵ The GISAXS images were recorded by a charge-coupled device (CCD) camera³⁶ (pixel size 22.5×22.5 μm^2) located 60 cm downstream the sample. An average of at least 100 images, each illuminated between 1 and 3 s, was taken. Before that, the dark current was subtracted from each frame.

III. RESULTS

The CEMS spectrum of an as-deposited sample at room temperature, Fig. 1(a), is an asymmetric line that can be decomposed into a broadened single line and a doublet labeled with M and I, respectively. The single line M (red) in Fig. 1(a) shows an isomer shift representative for metallic iron, which constitutes 69% of the film. The doublet (blue line), with its positive isomer shift, represents iron atoms at sites that are characterized by the broken translational symmetry, i.e., at the surface and Fe/MgO interface.²⁴ The CEMS spectrum demonstrates the lack of a long-range magnetic order, contrary to observations by Martinez Boubeta *et al.*,²⁶ who found a ferromagnetic order for films as thin as 4 ML. We explain this discrepancy as a result of different substrates used. The polished substrate, with high defect density, gives rise to nucleation of small islands. The interface energy may also be changed by surface contaminations, e.g., carbon impurities that cannot be removed from the surface of a polished substrate by standard procedures, favoring an island growth. Note that consequently, the nominal film thickness at which islands coalesce and superparamagnetism is blocked is increased.

Annealing of the sample up to 300 °C does not change the CEMS spectrum essentially [see Fig. 1(b)]. Most of the iron atoms do not exhibit long-range magnetic order. However, a careful analysis reveals a component with a broad distribution of the hyperfine magnetic field around $\langle B_{\text{hf}} \rangle = 13$ T [see sextet line (green) in Fig. 1(b)]. The appearance of that magnetic component is explained by the increase of the size of the superparamagnetic particles. The onset of the magnetically split spectrum means that some particles approach a critical dimension, for which the superparamagnetic relaxation time at room temperature is comparable with the characteristic time scale of the Mössbauer spectroscopy in the range of 10^{-10} – 10^{-7} s. Taking into account that the superparamagnetic relaxation can be described by an Arrhenius dependence with a pre-exponential factor³⁷ of 10^{-13} – 10^{-10} , the lower limit of the energy barrier for the superparamag-

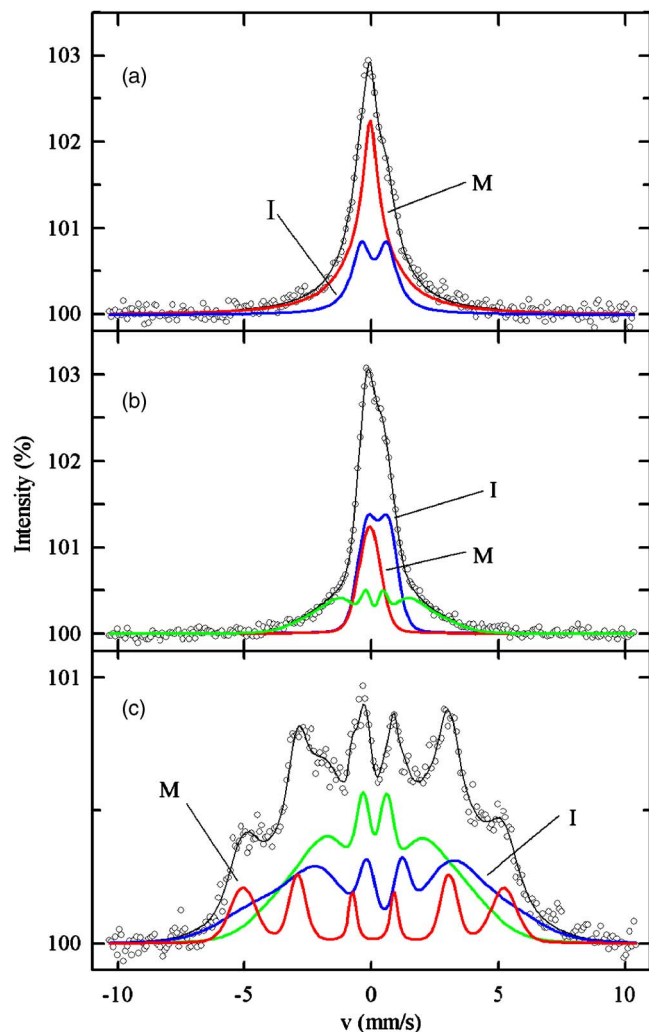


FIG. 1. (Color online) CEMS spectra of 5 ML ^{57}Fe on MgO(001); as prepared, measured at (a) room temperature; and after annealing for 1 h at 300 °C, measured at (b) room temperature and at (c) 80 K.

netic fluctuations can be estimated as $E_{\text{spm}} = K_{\text{eff}}V \approx 4k_{\text{B}}T$, where K_{eff} is the effective anisotropy constant and V is the volume of a superparamagnetic particle. That estimation of the particle size is quite ambiguous, as the effective anisotropy constant may include many different contributions (shape, interface, strain, etc.). Varying K_{eff} between K_1 of bulk iron²⁶ ($4.6 \times 10^4 \text{ J/m}^3$) and the fairly realistic value for particles on a surface of $1 \times 10^5 \text{ J/m}^3$, one ends up at a particle diameter between 7 and 3 nm, respectively. Interestingly, the coarsening of particles induced by annealing is accompanied by a slight increase of the interfacial/surface component (up to 40% after 1 h annealing at 300 °C) characterized by a high positive isomer shift. This means that either the coarsening goes hand in hand with a change of particle morphology, or an interfacial Fe/MgO process occurs.

At 80 K the spectrum becomes magnetically split [Fig. 1(c)]. Basically, the magnetic transition stems from the blocking of the superparamagnetism. It cannot be excluded, however, that for the smallest particles the onset of the ferromagnetic state, with the Curie temperature lying below room temperature, also contributes to the transition. The par-

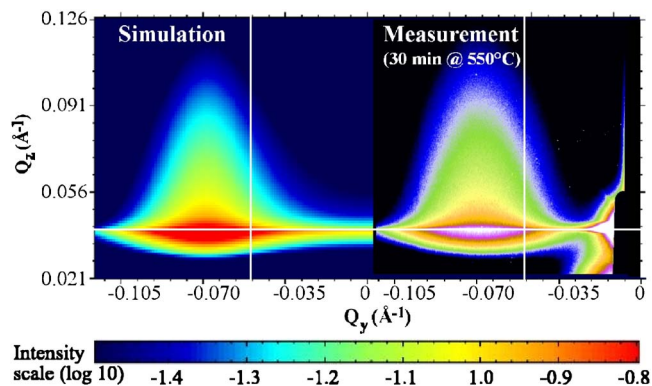


FIG. 2. (Color online) Measured GISAXS spectrum (right) of 5 ML Fe on MgO(001) after 30 min annealing at 550 °C and its simulation (left) assuming hemispherical island shape. The white lines show the positions of the two cuts used to fit the data, parallel and perpendicular to the surface.

ticles are far from being bulk metallic-like. Only 17% of the iron atoms display $B_{\text{hf}} = 31.9 \text{ T}$, close to the bulk value of 33 T, while the remaining ones, both metallic and surface/interfacial (as judged from the isomer shift), have B_{hf} considerably reduced and spread over a wide distribution. This may come either from not fully blocked superparamagnetism or from a core-shell morphology of the particles. The latter can be excluded as it is hardly to expect that for such a morphology an interface enhancement of magnetic moments can be detected.

More details on the particle morphology are obtained from GISAXS studies. As an example, Fig. 2 shows the two-dimensional GISAXS pattern collected after sample annealing at 550 °C for 30 min and a simulation assuming a hemispherical island shape. Rotating the sample by 45° with the rotation axis normal to the surface hardly changes the scattering image. This is proven by comparing the slices through the maxima for both azimuthal directions (see Fig. 3). Thus, the horizontal projection of the islands can exhibit neither a rectangular nor a hexagonal structure. Consequently, only island models with circular bases are taken into account for simulating the GISAXS data. Hence, the three different island shapes that are most likely are hemispheres, cylinders, and cones. Therefore, these shapes were used for simulations and subsequently for fits of two slices through the GISAXS images (Fig. 4). One slice was always parallel to the sample surface, along Q_y , and the other perpendicular, along Q_z . The fitting parameters applied simultaneously are the island radius r (nm), the height aspect ratio h/r , the mean distance D

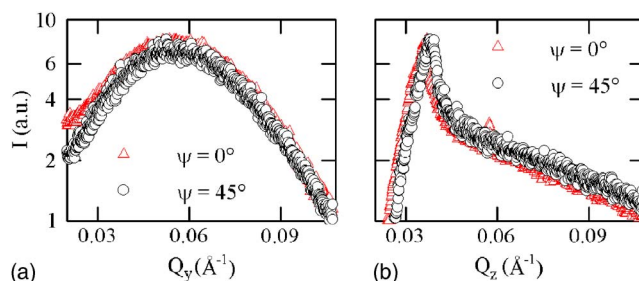


FIG. 3. (Color online) Slices through the maxima of the GISAXS images taken after annealing at 550 °C for 30 min (a) parallel and (b) perpendicular to the specimen surface for the two azimuthal angles $\psi = 0^\circ$ and $\psi = 45^\circ$.

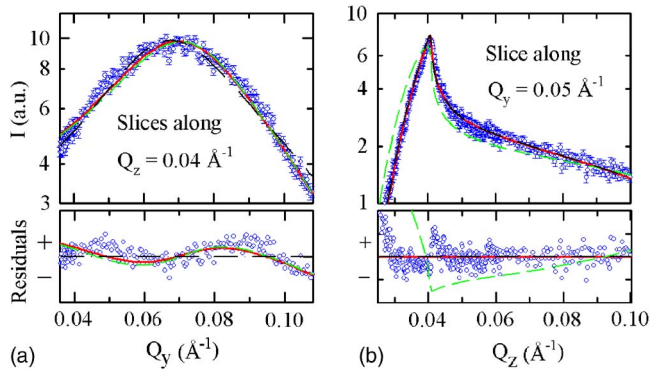


FIG. 4. (Color online) Slices (blue) through the GISAXS data from the sample annealed 30 min at 450 °C (a) parallel and (b) perpendicular to the surface. Three fits corresponding to a hemisphere (red solid line, $\chi^2_{\text{tot}}=2.6$), to a cylinder (green dashed line, $\chi^2_{\text{tot}}=12.4$), and to a cone (black dash-dotted line, $\chi^2_{\text{tot}}=11.0$) are shown. To outline the differences between the fits, the residuals are shown in the bottom panels, using the values for the cone as reference.

(nm), and the disorder parameter²⁷ ω (nm), which is a parameter describing the degree of small-range order between islands.

Although the fit of the slice along Q_z matches the experimental points quite well in case of a cylindrical form, along Q_y it does not. For cone-shaped islands, problems arise for the fit parallel to the surface, as the slope for high Q_y values is too steep. The best agreement is achieved by hemispherical island shapes. This can also be seen by comparing the χ^2 values for the different fit models (see bottom panels in Fig. 4). Consequently, all measurements are further analyzed presuming hemispherical shapes.

The island growth at different annealing temperatures is shown in Fig. 5. The increase of the mean distance D and the height h can be fitted, as suggested by, e.g., Jak *et al.*,³⁸ by an exponential function. For the growth behavior of the diameter d , two different temperature ranges have been considered. Between 100 °C and 200 °C the increase of the diameter is relatively high. Afterwards, at higher temperatures, it is strongly decelerated. Hence, the trend of the lateral island growth can be fitted by two exponential growth functions with different exponential parameters depending on the temperature. This is an indication for different growth modi.

Annealing the specimen at 550 °C results in a coarsen-

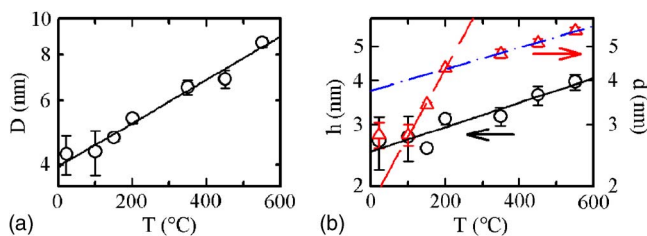


FIG. 5. (Color online) Dependence of the height h and the diameter d of iron clusters and their mean distance D on the annealing temperature. The line in (a) results from the linear regression of D . In (b) d is visualized by red triangles and h by black circles. The red dashed line represents the fit of d for low temperatures and the blue dash-dotted line for high temperatures. The black solid line illustrates the mean increase of h . Note that although exponential functions were fitted in (a) and (b), lines are straight due to the logarithmic scale of the ordinates.

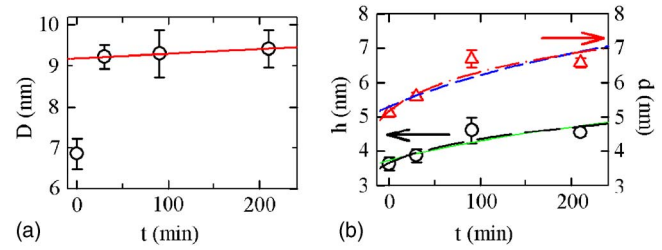


FIG. 6. (Color online) Temporal evolution of the height h and the diameter d of the iron clusters and their mean distance D at 550 °C. The spots at $t = 0$ min indicate the parameters of the sample before the 550 °C annealing, i.e., the sample was already annealed at 450 °C. The solid line in (a) shows the linear fit of the data detected after annealing for 30 min and longer. In (b) the triangles denote the island diameter and the circles the height. The dash-dotted (red) line and the long-dashed (black) line indicate cluster diffusion. The short-dashed (blue) and the solid (green) line correspond to the Ostwald ripening model.

ing of iron precipitates. The mean distance D between the islands grows dramatically in the first 30 min. Afterwards, the increase is decelerated. The data can then be fitted by a linear regression with a slope of 1.1 ± 0.1 pm/min [Fig. 6(a)]. The rise of the height h and the diameter d shows a much smoother behavior. Usually, in case of surface diffusion, the data are fitted by exponential functions. In order to distinguish between the two possible coarsening mechanisms, which are Ostwald ripening and cluster diffusion, the exponent m has to be evaluated. In case of Ostwald ripening, where single atoms diffuse toward the islands, m is supposed to be 4.^{39–41} For cluster diffusion it is expected to be 7.^{42–44} Given our results, we cannot unambiguously discriminate between Ostwald ripening and the cluster diffusion model as the proper coarsening mechanism. Figure 6(b) presents the differences between the measured data and the fitted functions based on the above two theories. An unambiguous proof of the relevant coarsening mechanism could be realized possibly by x-ray photon correlation spectroscopy. That method has already been applied in bulk materials.^{35,45}

The relations between the height h and the diameter d of the islands with respect to annealing time at 550 °C are presented in Fig. 7(a). The same is shown for different annealing temperatures in Fig. 7(b). The two points measured at room temperature and at 100 °C lie on the dashed blue line corresponding to full spheres. All other points are located in the area between the lines for full spheres and hemispheres.

Dependent on their positions the atoms of the iron is-

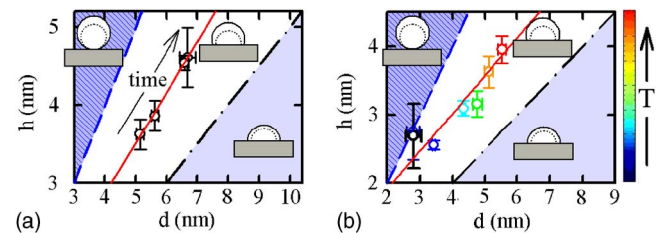


FIG. 7. (Color online) Evolution of the height h vs the diameter d of the islands. (a) displays the time dependence at 550 °C and (b) the temperature dependence between room temperature and 550 °C. The dash-dotted black line marks the positions where perfect hemispheres would be found. The dashed blue line refers to full spherical islands. These reference lines were obtained by purely geometrical considerations.

TABLE I. Fraction of the iron atoms at different sites of the islands. T is the annealing temperature, kept constant for 30 min each. M denotes the contribution of atoms at metallic sites, S at surface sites, and I at interface sites.

T (°C)	GISAXS			CEMS	
	M (%)	S (%)	I (%)	M (%)	$S+I$ (%)
RT	53±6	43±3	4±4	65±5	35±5
200	68±1	27±1	5±1	45±5	55±5
300	69±1	25±1	6±1	60±2	40±2
350	69±1	25±1	6±1		
450	70±3	25±2	5±1		
550	73±2	23±1	4±1		

lands have different electronic surroundings. This can be evaluated by CEMS. Iron atoms on the surface, inside the islands, and at the island-substrate interface have different chemical environments. This results in different components of the CEMS spectra with the fraction directly related to the fraction of atoms on the particular site. The proportions of the different chemical sites can also be distinguished by GISAXS assuming a body-centered-cubic iron structure and counting the number of atoms at the islands' surface, within the bulk and at the interface, taking into account the proper models for spheres and hemispheres, respectively. The surface atoms are lying within a shell with the thickness of the iron atom diameter. The interface atoms are the two ML of iron in contact with the substrate. Table I specifies the proportion of the different chemical sites obtained by GISAXS and CEMS. The discrepant values obtained by both methods can be explained by the fact that CEMS is sensitive to the chemical surrounding only and not to the shape itself. Annealing could be accompanied by a slight modification of the chemical surroundings of the surface or the interface atoms, for instance, due to oxidation by residual gases.

IV. DISCUSSION

The common, simple exponential functions that are usually used to distinguish between Ostwald ripening and cluster diffusion do not take into account size effects. Thus, these equations can be used only for relatively large islands.³⁸ At surfaces the growth exponent m , which is supposed to be 4 in the case of Ostwald ripening and 7 for cluster diffusion, increases for small precipitates. As the islands characterized in this paper are within the critical size range, diameter changes cannot be neglected. Hence, especially for short annealing times, the exponent m tends to exceed the values suggested by the established models. Another problem is that the assumed mean-field description holds only if a small fraction of the surface is covered with clusters. This approach ignores namely local variations, which are especially important in case of Ostwald ripening. In our case, the adatom concentration in the neighborhood of the precipitates can play a crucial role,^{46–50} because the island density lies in the range where the mean-field approximation is not applicable. Alternatively, the right coalescent mechanism can be figured out by evaluating the size distribution of the clusters.³⁸ Unfortunately, the obtained CEMS and GISAXS data did not allow to derive this distribution. An appropriate method to assess the right

mechanism of coarsening could be AFM. What can definitely be clarified by GISAXS is the isotropic spatial distribution and shape of the clusters, implying the diffusion constant of the iron particles to be independent of the crystallographic direction.

The sharp increase of the mean distance D during the first 30 min of the 550 °C annealing procedure is subsequently followed by a strongly decelerated slope. This can be explained by cluster diffusion in the early stages of coarsening and Ostwald ripening at later times, where the diameter d and height h are still growing although the distance D remains nearly constant. Consequently, during Ostwald ripening the number of iron atoms that contribute to the islands increases. This seems to be contradicting, since the total number of iron atoms at the surface must be constant. Moreover, the total number of atoms, derived from the GISAXS data, is less than the evaporated amount. These apparent discrepancies can be explained by the model of Martínez Boubeta *et al.*,²⁶ concerning the growth of iron clusters on cleaved MgO(001). They propose islands to be interconnected via iron bridges, which cannot be observed by the applied GISAXS method. Despite differences in sample preparation having a great impact on resulting structures, the above-mentioned model can be applied to the system under consideration in our studies. The saturation effect concerning the rise of D indicates iron nucleation mainly to emerge at defect sites.

Former results of magneto-optical Kerr effect measurements carried out on 3.5 ML iron on cleaved MgO(001) reported the formation of a continuous iron layer immediately after preparation. During annealing this layer breaks up into islands.²⁶ These observations could not be confirmed for 5 ML of iron on polished MgO(001). Here, isolated islands are already generated at room temperature, immediately after evaporation. Annealing enhances the island growth, whereas the island density decreases. Nevertheless, the assumptions concerning the cluster shape [disklike with $d=(11±3)$ nm and $h=1$ nm] are not likely to be correct for polished substrates. Our data yield higher, and laterally smaller, islands with hemispherical shapes. Reasons for distinct results are attributed to the higher impurity concentration on the surface of polished specimens; these impurities could be reduced, e.g., by annealing cycles in the presence of oxygen.⁵¹

In contrast to the Kerr spectra of iron on cleaved MgO,²⁶ CEMS measurements of 5 ML iron on polished MgO(001)

still indicate Volmer-Weber growth⁵² giving rise to superparamagnetic precipitates at small coverages. A similar effect was shown for even higher coverages by Cebollada *et al.*,⁵³ as also verified by CEMS, for 5 ML iron the Curie temperature lies below room temperature (see Fig. 1), although for bulk iron⁵⁴ it is 770 °C. This effect has also been found in Co/Cu(001).⁵⁵

V. CONCLUSION

We investigated the evolution of islands formed by evaporating ultrathin iron layers of only 5 ML onto polished MgO(001). The morphology was examined with respect to annealing procedures at temperatures between room temperature and 550 °C by CEMS and GISAXS. The CEMS results reveal the emergence of superparamagnetic iron clusters at the MgO(001) surface, where the Curie temperature is below 300 K. According to the literature, e.g., Ref. 26, the clusters are partly connected via iron bridges. The analysis of our GISAXS data yields the following information about the islands' morphology. At room temperature and up to 100 °C the island shape is that of a sphere; afterwards, it changes into a hybrid of a sphere and a hemisphere. Furthermore, the mean distance between islands rises mainly exponentially with annealing temperature.

The approach usually used for the analysis of standard catalysts, where the time-dependent particle growth is modeled by an exponential law with a straightforward interpretation of the growth exponent, cannot be applied to this system due to small cluster sizes. We relate the steep rise of the mean distance D between the islands in the early stages of annealing at 550 °C to cluster diffusion. After about 30 min, D grows only moderately, which we interpret as indication for nucleation at defect sites. Since the precipitates are still growing, this suggests Ostwald ripening via iron diffusion between the clusters. The isotropic distribution of the iron islands and their lateral dimensions imply an isotropic diffusion coefficient in all crystallographic directions of the MgO(001) surface.

ACKNOWLEDGMENTS

This work was financially supported by the EU-Specified Targeted Research Project DYNASYNC (Project No. NMP4-CT-2003-001516), the Austrian Federal Ministry for Education, Science and Culture (MDN Project No. GZ 45.529/2-VI/B/7a/2002), and the Austrian Science Foundation (FWF, Project No. P17775-N02).

¹B. M. Lairson, A. P. Payne, S. Brennan, N. M. Rensing, B. J. Daniels, and B. M. Clemens, *J. Appl. Phys.* **78**, 4449 (1995).

²C. Li and A. J. Freeman, *Phys. Rev. B* **43**, 780 (1991).

³J. Dekoster, S. De Groot, T. Kobayashi, and G. Langouche, *J. Magn. Magn. Mater.* **148**, 93 (1995).

⁴Y. Y. Huang, C. Liu, and G. P. Felcher, *Phys. Rev. B* **47**, 183 (1993).

⁵M. Hanson, C. Johansson, B. Nilson, P. Isberg, and R. Wappling, *J. Appl. Phys.* **85**, 2793 (1999).

⁶S. G. Kim, Y. Otani, K. Fukamachi, S. Yuasa, M. Nyvlt, and T. Katayama, *J. Magn. Magn. Mater.* **198–199**, 200 (1999).

⁷U. Ruediger, J. Yu, S. Zhang, and A. D. Kent, *Phys. Rev. Lett.* **80**, 5639 (1998).

⁸J. F. Lawler, R. Schad, S. Jordan, and H. van Kempen, *J. Magn. Magn. Mater.* **165**, 224 (1997).

⁹S. Adenwalla, Y. Park, G. P. Felcher, and M. Teitelmann, *J. Appl. Phys.* **76**, 6443 (1994).

¹⁰J. A. Venables, *Introduction to Surface and Thin Film Processes* (Cambridge University Press, Cambridge, UK, 2004).

¹¹B. M. Lairson, M. R. Visokay, R. Sinclair, S. Hagstrom, and B. M. Clemens, *Appl. Phys. Lett.* **61**, 1390 (1992).

¹²A. Subagyo, H. Oka, G. Eilers, S. Kazuhisa, and K. Mukasa, *Jpn. J. Appl. Phys., Part 1* **39**, 3777 (2000).

¹³S. M. Jordan, J. F. Lawler, R. Schad, and H. van Kempen, *J. Appl. Phys.* **84**, 1499 (1998).

¹⁴K. Thürmer, R. Koch, M. Weber, and K. H. Rieder, *Phys. Rev. Lett.* **75**, 1767 (1995).

¹⁵R. L. Schwoebel and E. J. Shipsey, *J. Appl. Phys.* **37**, 3682 (1966).

¹⁶S. J. Liu, H. Huang, and C. H. Woo, *Appl. Phys. Lett.* **80**, 3295 (2002).

¹⁷R. Moons, S. Blässer, J. Dekoster, A. Vantomme, J. D. Wachter, and G. Langouche, *Thin Solid Films* **324**, 129 (1998).

¹⁸G. Fahsold, A. Priebe, and A. Pucci, *Appl. Phys. A: Mater. Sci. Process.* **A73**, 39 (2001).

¹⁹G. Renaud, R. Lazzari, C. Revenant, A. Barbier, M. Noblet, O. Ulrich, F. Leroy, J. Jupille, Y. Borensztein *et al.*, *Science* **300**, 1416 (2003).

²⁰C. Revenant, F. Leroy, R. Lazzari, G. Renaud, and C. R. Henry, *Phys. Rev. B* **69**, 035411 (2004).

²¹F. Leroy, G. Renaud, A. Letoublon, R. Lazzari, C. Mottet, and J. Gonias, *Phys. Rev. Lett.* **95**, 185501 (2005).

²²I. Flis-Kabulska, B. Handke, N. Spiridis, J. Haber, and J. Korecki, *Surf. Sci.* **507–510**, 865 (2002).

²³G. Fahsold, A. Priebe, N. Magg, and A. Pucci, *Thin Solid Films* **364**, 177 (2000).

²⁴M. Zając, K. Freindl, K. Matlak, M. Ślęzak, T. Ślęzak, N. Spiridis, and J. Korecki, *Surf. Sci.* (to be published).

²⁵A. Subagyo, K. Sueoka, K. Mukasa, and K. Hayakawa, *Jpn. J. Appl. Phys., Part 1* **38**, 3820 (1999).

²⁶C. Martínez Boubeta, C. Clavero, J. M. García-Martín, G. Armelles, A. Cebollada, L. Balcells, J. L. Menéndez, F. Peiró, A. Cornet, and M. F. Toney, *Phys. Rev. B* **71**, 014407 (2005).

²⁷R. Lazzari, *J. Appl. Cryst.* **35**, 406 (2002).

²⁸S. K. Sinha, E. B. Sirota, S. Garoff, and H. B. Stanley, *Phys. Rev. B* **38**, 2297 (1988).

²⁹A. Holý, J. Kubuena, I. Ohlídal, K. Lischka, and W. Plotz, *Phys. Rev. B* **47**, 15896 (1993).

³⁰A. Holý and T. Baumbach, *Phys. Rev. B* **49**, 10668 (1994).

³¹D. K. G. de Boer, *Phys. Rev. B* **49**, 5817 (1994).

³²S. Dietrich and A. Haase, *Phys. Rep.* **260**, 1 (1995).

³³M. Rauscher, T. Salditt, and H. Spohn, *Phys. Rev. B* **52**, 16855 (1995).

³⁴M. Rauscher, R. Paniago, H. Metzger, Z. Kovats, J. Domke, H. D. Pfannes, J. Schulze, and I. Eisele, *J. Appl. Phys.* **86**, 6763 (1999).

³⁵B. Pfau, L.-M. Stadler, B. Sepiol, R. Weinkamer, J. W. Kantelhardt, F. Zontone, and G. Vogl, *Phys. Rev. B* **73**, 180101 (2006).

³⁶L.-M. Stadler, B. Sepiol, B. Pfau, G. Vogl, and F. Zontone, *Nucl. Instrum. Methods Phys. Res. B* **238**, 189 (2005).

³⁷G. T. Rado and H. Suhl, *Magnetism* (Academic, New York, 1963), Vol. III.

³⁸M. J. J. Jak, C. Konstapel, A. van Kreuning, J. Verhoeven, and J. W. M. Frenken, *Surf. Sci.* **457**, 295 (2000).

³⁹I. M. Lifshitz and V. V. Slyozov, *J. Phys. Chem. Solids* **19**, 35 (1961).

⁴⁰B. K. Chakraverty, *J. Phys. Chem. Solids* **28**, 2401 (1967).

⁴¹M. Zinke-Allmang, L. C. Feldman, and M. H. Grabow, *Surf. Sci. Rep.* **16**, 377 (1992).

⁴²K. Morgenstern, G. Rosenfeld, B. Poelsema, and G. Comsa, *Phys. Rev. Lett.* **74**, 2058 (1995).

⁴³S. V. Khare, N. C. Bartelt, and T. L. Einstein, *Phys. Rev. Lett.* **75**, 2148 (1995).

⁴⁴D. Kashchiev, *Surf. Sci.* **55**, 477 (1976).

⁴⁵L.-M. Stadler, B. Sepiol, R. Weinkamer, M. Hartmann, P. Fratzl, J. W. Kantelhardt, F. Zontone, G. Grübel, and G. Vogl, *Phys. Rev. B* **68**, 180101 (2003).

⁴⁶N. C. Bartelt, W. Theis, and R. M. Tromp, *Phys. Rev. B* **54**, 11741 (1996).

⁴⁷W. Theis, N. C. Bartelt, and R. M. Tromp, *Phys. Rev. Lett.* **75**, 3328 (1995).

⁴⁸G. R. Carlow, R. J. Barel, and M. Zinke-Allmang, *Phys. Rev. B* **56**, 12519 (1997).

⁴⁹G. Rosenfeld, K. Morgenstern, I. Beckmann, W. Wulfhekel, E. Lægsgaard, F. Besenbacher, and G. Comsa, *Surf. Sci.* **402–404**, 401 (1998).

⁵⁰M. S. Hoogeman, M. A. J. Klik, R. van Gestel, and J. W. M. Frenken, *J. Phys. Condens. Matter* **11**, 4349 (1999).

⁵¹S. S. Perry, H. I. Kim, S. Imaduddin, S. M. Lee, and P. B. Merrill, *J. Vac. Sci. Technol. A* **16**, 3402 (1998).

⁵²M. Volmer and A. Weber *Z. Phys. Chem., Stoechiom. Verwandtschaftsl.* **119**, 277 (1926).

⁵³F. Cebollada, A. Hernando-Mañeru, A. Hernando, C. Martínez Boubeta,

A. Cebollada, and J. M. González, *Phys. Rev. B* **66**, 174410 (2002).

⁵⁴*Binary Alloy Phase Diagrams*, edited by T. B. Massalski (American Society for Metals, Metals Park, OH, 1986).

⁵⁵C. M. Schneider, P. Bressler, P. Schuster, J. Kirschner, J. J. de Miguel, and R. Miranda, *Phys. Rev. Lett.* **64**, 1059 (1990).